AIMS Energy

AIMS Energy, 14(1): 212–234.
DOI: 10.3934/energy.2026009
Received: 16 October 2025
Revised: 31 December 2025
Accepted: 26 January 2026
Published: 11 February 2026

https://www.aimspress.com/journal/energy

Research article

Robust prediction of lithium-ion battery temperature using wavelet scattering and deep learning

Mohamed M. A. Hassan, Hatem Kayed and Bassam Adel*

Mechanical Power Engineering Department, Faculty of Engineering, Cairo University, Cairo, Egypt.

* **Correspondence:** Email: Bassamadel08010@gmail.com, BassamaAdelPM@outlook.com; Tel: +201007999965.

Abstract: Lithium-ion batteries are essential for electric vehicles and energy storage systems; nevertheless, inconsistent temperature distributions jeopardize their safety and reliability, potentially resulting in thermal runaway. Thus, precise temperature forecasting models are crucial for enhancing performance and guaranteeing operational safety. In this research, we present a hybrid framework that combines the Wavelet Scattering Transform (WST) with Long Short-Term Memory (LSTM) neural networks to predict battery temperature distributions. The methodology was validated using datasets from the NASA Ames Prognostics Center of Excellence (PCoE), which included authentic cycle data for voltage, current, and temperature. To guarantee reliability, model predictions were calibrated and assessed using three methods: RAW outputs, bias correction, and Poly2. The proposed WST-LSTM framework showed improved stability and consistency relative to the raw-signal LSTM baseline, supporting its suitability for thermal-safety evaluation and battery-management applications. The proposed framework was implemented in MATLAB/Simulink for an electric-vehicle battery model, thereby validating its applicability to real-world automotive platforms. This study emphasizes forecasting temperature at a specific sensor point rather than reconstructing the temperature field. The suggested WST-LSTM model predicted the temperature trajectory at this location utilizing electrical and environmental signals.

Keywords: electric vehicles; lithium-ion batteries; Wavelet Scattering Transform (WST); LSTM; temperature prediction

1. Introduction

Lithium-ion batteries (LIBs) are widely used in consumer devices and electric vehicles due to their high energy density, minimal self-discharge, extended cycle life, and lack of memory effect [1]. Systems for energy storage based on LIBs are also essential for the widespread adoption of renewable energy sources [2]. Because the LIB is an electrochemical system, its performance and safety are directly impacted by its operating temperature.

In addition to charging and discharging, prolonged exposure to excessively high or low temperatures can shorten battery lifespan and accelerate deterioration [3]. Moreover, thermal runaway in batteries caused by exposure to extremely high temperatures can result in fires or even explosions [4]. Therefore, it is essential to understand, predict, and enhance the thermal behavior, heat transfer processes, and temperature of LIBs to ensure their safety and optimal performance [5].

Lithium-ion batteries are essential for electric vehicles (EVs) and energy storage systems due to their high energy density and long cycle life. Nonetheless, inconsistent temperature distributions within battery cells undermine safety and reliability, frequently hastening degradation and increasing the risk of thermal runaway. Thus, precise temperature forecasting is essential to ensuring thermal safety, prolonging battery lifespan, and improving the effectiveness of battery management systems (BMS).

Predicting and managing battery temperature requires an understanding of the fundamental principles of heat generation in LIBs. According to its principles, the internal heat generated in LIBs during operation can be divided into four major sources: Heat from mixing, side reactions, irreversible heat production, and reversible heat generation [6]. Ohmic and kinetic losses are the sources of irreversible heat generation, whereas entropy changes in electrochemical processes during battery charging and discharging are the sources of reversible heat generation [7]. Although side reactions in lithium-ion batteries, such as chemical interactions between the electrolyte and the cathode or anode active materials, are often negligible at standard operating temperatures, they become more pronounced at higher temperatures. The heat produced by these exothermic side reactions may further increase battery temperature. This self-accelerating thermal feedback loop, in which elevated temperatures facilitate additional side reactions that generate more heat, is referred to as thermal runaway (TR) [8]. This is a significant safety issue for LIB systems. The specific triggers and fundamental processes of TR are well established in the literature [9–11]. Finally, the heat of mixing refers to the thermal energy released due to changes in local composition and the energy of electrode particles during lithium-ion diffusion under concentration gradients. This phenomenon becomes pronounced at elevated charge/discharge rates, whereas it is frequently insignificant at lower rates [12]. Thus, understanding the heat-generation processes of lithium-ion batteries and developing predictive models of heat-generation rates across operating conditions for various battery types is essential for designing effective battery thermal management systems.

Lithium-ion (Li-ion) batteries' high energy density, extended cycle life, and comparatively low self-discharge rates have made them the industry standard for energy storage in electric vehicles (EVs), portable gadgets, and stationary energy systems [13]. However, internal thermal behavior significantly affects their performance and safety, despite these benefits. The cells' internal temperature fields are non-uniform, which accelerates degradation processes, reduces functional capacity, and can trigger thermal runaway events, hazardous [14,15] phenomena. For long-term reliability and battery management systems (BMS), precise prediction of the temperature field is essential.

Conventional methods for battery thermal modeling often rely on equivalent circuit models (ECMs) or computational fluid dynamics (CFD) simulations [16]. Although these approaches provide physical interpretability, they are constrained by high computational costs, complex parameterization requirements, and challenges in generalizing across operating conditions. Conversely, data-driven methodologies have emerged as formidable alternatives, leveraging historical operational data to predict thermal and electrochemical states with high precision [17]. Deep learning methodologies, including convolutional neural networks (CNNs), LSTM networks, and bidirectional LSTMs (Bi-LSTMs), have shown promising results in modeling the nonlinear temporal dynamics of battery signals [18,19]. Wang et al. [20] developed a CNN-Bi-LSTM—Attention model for temperature prediction in Li-ion batteries, achieving significant improvements in accuracy over traditional methods.

Moreover, wavelet-based techniques have been investigated for feature extraction in battery diagnostics. The WST offers translation-invariant and multi-scale representations of signals, facilitating the robust characterization of voltage and current variations [21]. Ramamurthy et al. [22] used WST in conjunction with spiking graph transformer networks for battery health monitoring, achieving improved accuracy and generalization. These advancements underscore the potential to integrate wavelet-based spectrum representations with deep learning systems to enhance predictive performance.

Although significant progress has been made in modeling and predicting the thermal behavior of lithium-ion batteries, several critical gaps remain. Physics-based thermal models provide interpretability but are computationally expensive and require extensive parameterization, making them impractical for real-time applications. Data-driven approaches, including CNN, LSTM, and Bi-LSTM models, have shown promise for sequence learning. Yet, most researchers focus on state-of-charge (SOC), state-of-health (SOH), or capacity prediction rather than explicit temperature-field prediction. Moreover, while WST has demonstrated strong capabilities for robust feature extraction in power systems and battery diagnostics, it has not been systematically applied to the thermal prognostics of lithium-ion batteries. Finally, few researchers have validated their models on benchmark datasets such as the NASA Ames PCoE battery dataset [23], which are critical for reproducibility and comparability. These limitations highlight the need for a hybrid framework that integrates WST for spectral feature extraction with LSTM for temporal modeling, targeting accurate and robust prediction of battery temperature fields. In this study, we focus on sensor-level temperature forecasting at a single measurement location, which represents the practical thermal indicator commonly used in Battery Management Systems (BMS), rather than reconstructing a spatial temperature field.

This paper's principal contributions are summarized as follows:

1. An innovative method for forecasting lithium-ion battery (LIB) temperature distributions by integrating WST for resilient spectral feature extraction with LSTM networks for temporal sequence analysis is presented.
2. The proposed WST-LSTM system is the first effort to implement wavelet scattering on real-world NASA Ames benchmark datasets (B0005-B0018), further applied to a MATLAB/Simulink-based electric vehicle battery model, guaranteeing authenticity and repeatability of the outcomes.
3. Extensive trials indicate that the WST-LSTM model markedly surpasses traditional LSTM trained on raw data for accuracy, robustness, and generalization under varying cycle settings.

4. This study confirms the efficacy of hybrid data-driven models in representing thermal dynamics, providing a viable approach to improving thermal safety and degradation evaluation in lithium-ion (BMS).

In this paper, we present a hybrid framework that integrates the Wavelet Scattering Transform (WST) for translation-invariant feature extraction with Long Short-Term Memory (LSTM) networks to address these shortcomings. A polynomial calibration (Poly2) phase is subsequently implemented to rectify non-linear residuals and improve stability. The framework is validated on the NASA Ames Prognostics Center of Excellence (PCoE) dataset and implemented in a MATLAB/Simulink-based electric-vehicle battery model, demonstrating its practical applicability in real-world scenarios. In this work, the focal variable is the temperature recorded at a single location on the cell surface, which serves as the primary thermal indicator used by the BMS. Our objective is to forecast temperature at the sensor level rather than reconstruct a two- or three-dimensional temperature field.

The document is organized into five major sections. In Section I, we present our context, rationale, and aims. In Section II, we examine pertinent literature, summarize investigations on battery temperature forecasting, and highlight shortcomings. In Section III, we delineate the suggested technique, encompassing the WST-LSTM architecture and the calibration strategies (RAW, Bias correction, and Poly2). In Section IV, we outline the experimental configuration, dataset characterization (NASA Ames cells B0005, B0006, B0007, and B0018), and the results acquired, accompanied by a comparison study with prior research. In Section V, we conclude by highlighting the benefits of the proposed methodology and delineating potential research avenues, specifically in (BMS) and electric vehicles.

2. Related Work

The forecasting of thermal behavior in lithium-ion batteries has been thoroughly examined using physics-based and data-driven methodologies. Physics-based models, such as electrochemical-thermal coupled models and computational fluid dynamics (CFD) simulations, offer interpretability and comprehensive insights into heat generation and propagation mechanisms [14]. However, they often require intricate parameter identification and incur substantial computational costs, thereby limiting their practical application in real-time (BMS) [16].

Researchers have increasingly used the WST for modeling energy systems and power signals, owing to its robustness to temporal shifts, resilience to high-frequency noise, and translation-invariant multi-scale representations. A study indicated that WST-based feature matrices markedly improve the classification of power-system disturbances compared with conventional wavelet and time-domain approaches [24]. Researchers conducting a study employed wavelet-scattering-enhanced neural network models for short-term load forecasting in distribution networks [25], demonstrating that converting raw electrical data into scattering-domain features improves prediction robustness under varying operational conditions. In contrast to these applications, we amalgamate WST-derived thermal characteristics with an LSTM framework and incorporate a quadratic (Poly2) bias-correction phase.

To address these constraints, data-driven methodologies have garnered considerable interest. Initial researchers have used autoregressive models and support vector regression to estimate battery temperature [17]. Moreover, deep learning techniques, including convolutional neural networks (CNN), recurrent neural networks (RNN), and LSTM, have been extensively used in battery prognostics. In Ref. [20], a CNN-Bi-LSTM—Attention mechanism was proposed for temperature field prediction, achieving higher accuracy than traditional approaches. Likewise, hybrid deep models have been used to estimate remaining usable life (RUL) and state-of-health (SOH), thereby reinforcing the benefits of sequence learning architectures in battery applications [26,27].

Wavelet-based signal analysis has developed as an effective method for processing non-stationary and nonlinear battery signals. In Ref. [22], the WST was used for robust feature extraction in battery diagnostics, demonstrating robustness to noise and fluctuation in operating circumstances. In addition to batteries, WST has been successfully used in several energy-related sectors. The researchers in Refs. [28] and [29] presented performance analyses of WST-based feature matrices for power system disturbance classification, and those in Ref. [28] introduced an innovative WST-LSTM framework for microgrid fault detection and classification, demonstrating the significant potential of wavelet scattering in conjunction with deep learning. These results strongly support extending WST-LSTM models to include battery thermal-field prediction.

Notwithstanding these advancements, only a limited number of researchers have examined the integration of wavelet scattering with temporal deep learning frameworks for forecasting temperature distributions in lithium-ion batteries. Furthermore, few researchers have validated these techniques on benchmark datasets, such as the NASA Ames PCoE battery dataset, which are widely used in prognostics research [23]. This disparity underscores the need for a hybrid framework that leverages WST's spectral invariance and LSTM's temporal modeling capabilities, which underpin this research.

Investigations have improved the capabilities of battery temperature-field prediction using hybrid and deep learning approaches. Wang et al. [30] proposed a CNN-BiLSTM network for thermal field estimation in lithium-ion modules. They achieved an RMSE of approximately 0.10 °C for simulated pack-level measurements. Xu et al. [31] developed a nonlinear kernel-based dimensionality reduction approach combined with a BP neural network. They reported an R^2 greater than 0.99 for reconstructing internal temperatures. Although these studies rely on simulation-generated thermal fields rather than accurate experimental signals, they are valuable for providing important context for comparison. Our investigation differs from other studies in that we focus on actual NASA PCoE sensor-level temperature profiles and employ WST-based hierarchical feature extraction combined with Poly2 calibration.

3. Dataset and preprocessing

1. Source

In this study, we employed the NASA Ames PCoE Li-ion battery dataset (cells B0005, B0006, B0007, B0018). The experiments were conducted under controlled laboratory conditions at approximately 24 °C.

2. Cells

Commercial 18650-format lithium-ion cells. Each MAT file stored multiple charge-discharge cycles as MATLAB structs.

3. Signals per cycle

The dataset provided terminal voltage V [V], current I [A], measured surface temperature T [°C], and time t [s], together with metadata, including cycle index, cycle type (charge/discharge), and ambient temperature.

4. Selection

Only cycles with complete V, I, T measurements and a duration exceeding the required modeling horizon ($W + \tau = 110$ seconds in this study) were retained. Incomplete or corrupted cycles were discarded to ensure data integrity and consistency. In this study, a forecasting horizon of $\tau = 20$ seconds was adopted, which aligned with the short-term prediction ranges (10–30 s) commonly reported in the literature for real-time thermal management of lithium-ion batteries [20,22]. Figure 1 shows a schematic representation of the supervised learning setup. The model observed 90 seconds of past data (input window W) and predicted the cell temperature 20 seconds ahead (prediction horizon τ).

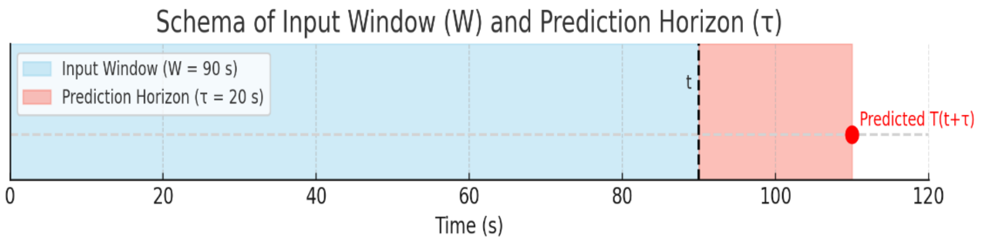

Figure 1. Input window ($W = 90$ s) and prediction horizon ($\tau = 20$ s).

5. Resampling

Raw irregular samples were linearly interpolated to a uniform sampling frequency of 1 Hz, producing synchronized sequences $V(t)$, $I(t)$, and $T(t)$.

6. Derived channels

In addition to the raw voltage and current inputs, several physics-informed features were derived to enhance the model's representation power. Specifically, power ($P = V \times I$) was included to capture Joule heating effects; current and voltage derivatives (dI/dt, dV/dt) were used to characterize transient dynamics; and state of charge (SOC) was estimated via Coulomb counting to provide context on the battery's operating condition. These engineered channels enriched the feature space and have been demonstrated to improve thermal prediction performance, as corroborated by studies on Joule heating and thermal runaway mechanisms [9], surveys on machine learning-assisted thermal management [32], and hybrid CNN-BiLSTM frameworks incorporating SOC for battery modeling [33].

7. Normalization

All features were normalized by z-score using the training-set statistics (μ, σ), and the same normalization was applied to the validation and test sets to prevent data leakage.

8. Target

The prediction target was the future temperature measured at the sensor location, defined as $y(t) = T(t + \tau)$, $\tau = 20$ seconds.

9. Split

A group-aware protocol was applied: 70% of cycles for training, 15% for validation, and 15% for testing. To avoid leakage, windows originating from the same physical cycle were always assigned to the same split.

10. Quality control

Non-finite samples were removed, duplicate timestamps were eliminated, and short cycles were discarded. Across all four cells, the pipeline generated =60,000 windowed sequences, partitioned into 42,000 for training, 9,000 for validation, and 9,000 for testing.

Table 1. Summary of the NASA Ames Li-ion battery cells used in this study.

Cell ID	Cycles parsed	Valid cycles used	Windows generated	Role in experiment
B0005	168	60	22,000	Training + Validation
B0006	132	60	14,000	Testing (generalization)
B0007	124	60	12,000	Testing (generalization)
B0018	120	60	12,000	Training + Validation
Total	544	240	60,000	Split: 70% Train, 15% Val, 15% Test

Notes: Only the first 60 cycles per file were used to control dataset size (maxCyclesPerFile = 60). The sliding window protocol (W = 90 s, hop = 10 s, horizon = 20 s) yields ~60 k supervised samples. The split is group-aware by cycle to ensure reproducibility and prevent leakage.

Table 1 summarizes the dataset characteristics of the NASA Ames Li-ion battery cells used in this study. A total of four battery cells (B0005, B0006, B0007, and B0018) were analyzed, providing a combined total of 240 valid cycles and 60,000 generated windows. The data split follows a 70% training, 15% validation, and 15% testing ratio, with specific cells designated for generalization testing to evaluate model performance on unseen data.

Figure 2 is an illustration of the dataset splitting strategy. The processed dataset was divided into 70% training, 15% validation, and 15% testing using a group-aware protocol to ensure that all windows from the same cycle were assigned to the same subset, thereby preventing data leakage. Figure 3 shows a flow diagram of the dataset preprocessing pipeline, illustrating the sequential steps:

Data cleaning, resampling, cycle filtering, sliding window segmentation, feature engineering, normalization, and data splitting.

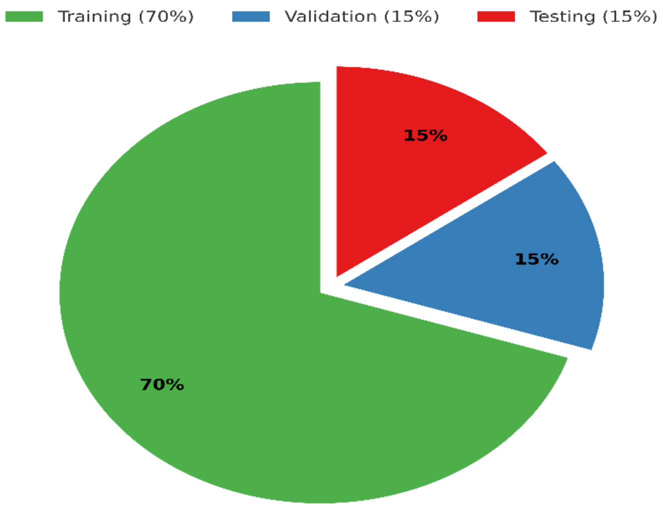

Figure 2. Data splitting strategy.

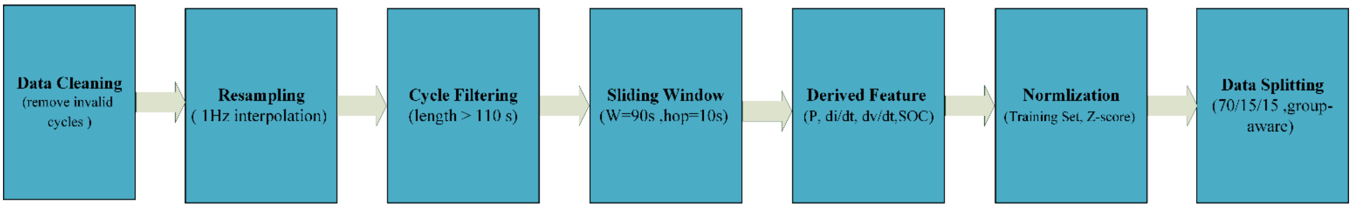

Figure 3. Flow diagram of the dataset preprocessing pipeline.

4. Methodology

In this section, we delineate the feature-extraction and modeling methods used to forecast the temperature distributions of lithium-ion batteries. The procedure commences with the data preprocessing of the NASA Ames benchmark dataset, followed by feature extraction with the WST. The collected scattering coefficients were subsequently fed into LSTM networks for temporal sequence learning, followed by post hoc calibration to improve predictions.

4.1. Feature extraction with wavelet scattering transform

The WST, created by Bruna and Malat in 2012, computes a locally translation-invariant representation of real-valued signals that is robust to time-warping deformations and applicable in various signal processing and machine learning contexts. The translation-invariant representation is derived by sequentially applying wavelet convolutions, modulus operators, and low-pass filters, which average the amplitudes of the iterated wavelet coefficients [34–38]. WST integrates the robustness of conventional signal-processing techniques with the complexity of deep neural networks. It produces feature vectors that are robust to noise, invariant to time shifts, and stable under time-warping deformations, yielding significant performance gains in classification tasks [39,40].

The WST offers translation invariance, meaning that temporal shifts do not affect the retrieved features. Furthermore, it guarantees stability against deformation and resilience to noise, thereby enhancing the reliability of the representation. Moreover, it autonomously acquires multi-scale frequency content, providing a comprehensive and adaptable characterization of the input signal.

In the medical domain, WST has been used as an effective feature-extraction tool for X-ray COVID-19 detection [41], to categorize interictal and preictal EEG data [42], to evaluate wearable electrocardiogram quality [43], and for glaucoma identification [44], among others. Furthermore, WST exhibits commendable efficacy in chemical applications; Mallat et al. [45] presented its use for the classification of organic molecules. The advancement of WST applications in the electrical engineering sector remains sluggish. Rohan [46] has developed a method using WST to diagnose mechanical components of industrial robots, enabling defect detection through feature extraction of the current signal. In Ref. [47], the various mixed faults of quadcopter constructions were accurately classified. A classification system for nonintrusive appliance load monitoring-based WST feature extraction achieves an accuracy of up to 99.98%, as proposed in Ref. [48]. Superior fault diagnosis accuracy compared to alternative methods in the literature; Varun Khemani et al. introduced a fault detection strategy for analog circuits, rotating machinery bearings, and gear problems utilizing WST features [40]. An approach for detecting bearing faults in rotating machines based on WST feature extraction is presented in Refs. [49,50]. A feature matrix is used in these applications, employing one or more WST coefficients based on the characteristics of the examined signal components.

The WST mathematical algorithm and its structure, akin to convolutional neural networks, were proposed by Bruna and Malat in 2012. As illustrated in Figure 4, the real-valued signal was analyzed using WST through three consecutive computational stages; the convolution step assessed the signal's similarity with wavelets of varying frequency and scale. Subsequently, the modulus nonlinearity process extracted the amplitude modulation of the convolved signal, thereby enabling the extraction of higher-order modulations. The averaging step functioned as a form of pooling that enforced time-shift invariance. For the intricate signal:

$$f(t) = f_r(t) + j\, f_i(t) \tag{1}$$

The modulus operator is defined as:

$$|f(t)| = \sqrt{f_r(t)^2 + f_i(t)^2} \tag{2}$$

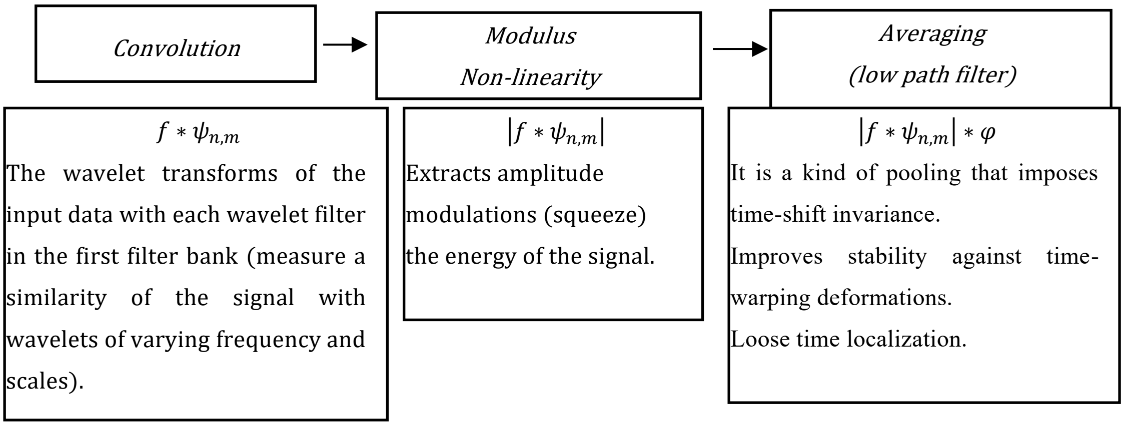

The wavelet transforms of the input data with each wavelet filter in the first filter bank (measure a similarity of the signal with wavelets of varying frequency and scales).

Extracts amplitude modulations (squeeze) the energy of the signal.

It is a kind of pooling that imposes time-shift invariance.
Improves stability against time-warping deformations.
Loose time localization.

Figure 4. WST mathematical steps.

f(t): The input signal.
φ(t): The scale function (low-pass filter).
$\psi_{n,m}$: The wavelet filter at scale n and orientation/frequency m.
$f * \psi_{n,m}$: Convolution of the input signal with the wavelet filter.
$|f * \psi_{n,m}|$: Modulus (non-linearity) applied to the wavelet transform, extracting amplitude modulations.
$(|f * \psi_{n,m}|) * \varphi$: Averaging (low-pass filtering) of the modulus, producing scattering coefficients with time-shift invariance.

The squares of the real and imaginary components of the signal convolved with the invariance scale function yield a modulated coefficient that is independent of the temporal presence of disturbances. The next stage was averaging (low-pass filtering), which could be regarded as a form of pooling that performed an implicit downsampling, thereby reducing the dimensionality of the feature map. This enhanced the model's robustness to fluctuations in feature positioning within the input signal and increased its stability against temporal deformation. The exact temporal localization was compromised throughout the averaging process. Therefore, the WST demonstrated the ability to handle non-stationary signals by providing stable, invariant representations. Battery signals were nonlinear and non-stationary. To capture their spectral-temporal dynamics robustly, the WST was applied:

- WST produces translation-invariant, multi-scale scattering coefficients from each signal.
- Parameters: invariance scale ≈ 10 s, quality factors Q = [1,1].
- The scattering coefficients provide a fixed-length representation, robust to noise and shifts, enriching the feature space compared to raw signals.
- Channels processed: V, I, P, dI/dt, SOC.

The hyperparameters of the scattering transform in this study were explicitly articulated to enable replication of the work. To account for slow thermal trends and high-frequency transient components generated by dynamic loading, first- and second-order scattering paths were selected. The quality factor Q was set to 8 to provide a good balance of time-frequency resolution suitable for the thermal dynamics of lithium-ion batteries. An invariance scale of about 10 seconds was employed to match the main thermal time constant observed in the NASA PCoE profiles, thus enabling the representation to retain significant slow fluctuations while reducing high-frequency noise. The resulting scattering coefficients formed a compact and structured feature vector, the size of which was inherently determined by the selected scattering orders, filter bank configuration, and invariance scale. There were no additional dimensionality-reduction methods applied as WST inherently produced stable, energy-normalized coefficients that could be used directly for sequence modeling with LSTM.

4.2. Model architecture

LSTM, developed by Hochreiter and Schmidhuber [51], was designed to mitigate the vanishing gradient problem in recurrent neural networks (RNNs) and is used to learn and process information across extended data sequences. LSTMs employ specialized gates, namely the forget gate and the output gate, to efficiently manage gradient flow. The LSTM architecture is a variant of RNN that, when integrated with an appropriate gradient-based learning algorithm via a sequence of gates, is more effective at identifying significant temporal patterns in time series data. Time series data characterized by repetition can be reliably predicted using LSTM networks.

The construction of a conventional RNN repeating module is exceedingly straightforward, comprising solely a single tanh layer. The fundamental architecture of LSTMs is more intricate than that of RNNs, consisting of a sequence of LSTM cells, each equipped with a set of gates that execute distinct functions, specifically the input gate, forget gate, and output gate, as illustrated in Figure 5. The three gates meticulously regulate the LSTM to incorporate or exclude information from the cell state, enabling LSTMs to preserve or discard pertinent details selectively. The output of each LSTM cell is passed to the next cell in the network, allowing the LSTM to analyze consecutive data over several time steps. This makes it highly beneficial for comprehending and forecasting patterns in sequential data, encompassing language modeling, speech recognition, image analysis, signal classification, and, more recently, power system problem diagnosis [52–56].

The composition consists of a layer of sigmoid and hyperbolic tangent functions. The sigmoid layer produces values between 0 and 1, indicating the extent to which each component is enabled to flow through. A value of zero signifies total inhibition, while a value of one denotes total activation.

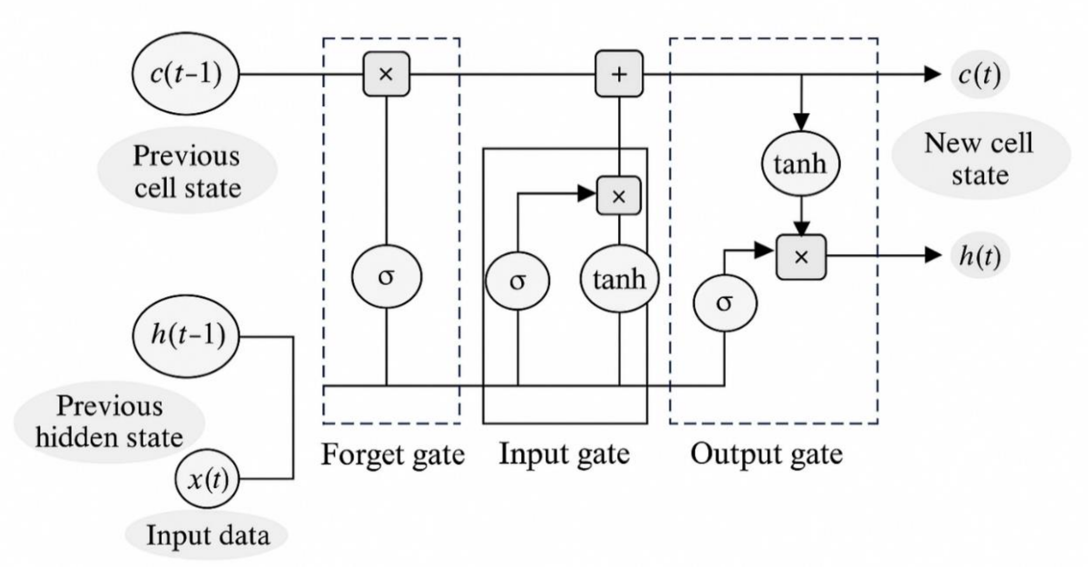

Figure 5. Architecture of the LSTM network cell.

Figure 5 depicts the progress of a time series dataset *X*, with a time step length *t*, as it proceeds through an LSTM layer as follows:

If the weight matrix and bias matrix are given by:

$$w = \begin{pmatrix} w_f \\ w_i \\ w_n \\ w_o \end{pmatrix}, \quad b = \begin{pmatrix} b_f \\ b_i \\ b_n \\ b_o \end{pmatrix} \tag{3}$$

Then, the new cell state is given by:

$$c(t) = \left[\sigma\left(w_f[h(t-1), x(t)] + b_f\right) * c(t-1)\right] + [\sigma(w_i[h(t-1), x(t)] + b_i) * \tanh(w_n[h(t-1), x(t)] + b_n)] \tag{4}$$

While the new hidden state is given by:

$$h(t) = \sigma(w_o[h(t-1), x(t)] + b_o) * \tanh\,(c(t)) \tag{5}$$

where c(t-1) is the previous cell state, h(t-1) is the last hidden state, c(t) is the new cell state, h(t) is the latest hidden state, and σ and tanh are the sigmoid and tanh functions.

It can be seen that two types of normalizing equations are used in the LSTM. The first part of Eq (4) computes the forget gate output using a sigmoid function, which determines whether to exclude or retain data. The sigmoid function determines which parts of the previous production should be deleted. By the two normalizing equations, the sigmoid (0, 1) and the tanh (−1, 1), the second part of Eq (4) is calculated. The sigmoid layer determines whether incoming information should be updated or ignored, while the tanh function assigns a weight to the incoming data, determining its relevance. The two values are multiplied to determine the new cell state. The new memory is subsequently added to the old memory, yielding C(t), as shown in Eq (4). Using the sigmoid and tanh functions, the new hidden layer is calculated as in Eq (5). The first part of Eq (5) is similar to the forget gate operation, which determines which parts of the cell state are transferred to the output and which are ignored. Then, the activation of the next hidden state is provided. The collected WST features were input into an LSTM-based network. The architecture is encapsulated in Table 2.

Table 2. Model architecture of the proposed WST-LSTM framework.

Layer	Type/Units	Description/Function
Input layer	Sequence input	Receives WST feature sequences (V, I, P, SOC, dI/dt)
LSTM layer 1	128 units	Captures long-term temporal dependencies
Dropout layer 1	p = 0.25	Prevents overfitting by randomly deactivating neurons
LSTM layer	64 units (bidirectional)	Learns both forward and backward dependencies
Fully connected layer	64 neurons + ReLU	Maps recurrent features into a compact representation
Dropout layer 2	p = 0.25	Adds regularization to enhance robustness
Output regression layer	1 neuron (linear)	Produces the predicted temperature value

4.3. Training strategy

The model was trained in supervised mode with the configuration shown in Table 3.

Table 3. Training configurations of the proposed WST-LSTM model.

Parameter	**Value/Setting**	**Notes**
Loss function	Mean Squared Error (MSE)	Measures prediction error
Optimizer	Adam	Initial LR = 0.001; step decay 0.5 every 10 epochs
Epochs	80	Early stopping with patience = 5
Batch size	64	Balanced efficiency & stability
LSTM hidden units	128 (1st LSTM)	Temporal dependency learning
Dropout	0.25	Regularization against overfitting
L2 regularization	1e−4	Weight decay
Validation split	15% (group-aware by cycle)	Prevents leakage across cycles

To assess the feasibility of the proposed WST-LSTM framework, a computational efficiency study was conducted. During both training and inference, the model exhibited low computational cost. The average training time per epoch was very short due to the small LSTM architecture; however, inference took only a few milliseconds per prediction window. The WST-LSTM model had a small number of parameters and was highly memory-efficient during inference; thus, it was well-suited to real-time or on-board Battery Management System (BMS) applications. The suggested method, compared with the simple LSTM, incurred a slight computational overhead but improved prediction performance substantially.

4.4. Evaluation and calibration

To ensure reliable results, three post-hoc calibration strategies were tested on model outputs:

1. RAW: Direct predictions without adjustment.
2. Bias correction: Constant offset based on validation residuals.
3. Poly2: Second-order polynomial mapping fitted on validation predictions.

The method with the lowest validation RMSE was selected for final reporting. Performance was assessed using RMSE, MAE, and R^2 on the test set.

4.5. Framework overview

The comprehensive methodological approach is summarized in Figure 6. The pipeline commenced with the NASA Ames benchmark datasets, followed by data preprocessing, including cleaning, resampling, cycle filtering, sliding-window segmentation, feature engineering, and normalization. Signal processing transformed the WST to yield translation-invariant and resilient spectral characteristics. The characteristics were subsequently input into the LSTM/BiLSTM-based network, which captured long-term temporal dependencies. Ultimately, post hoc calibration techniques (RAW, Bias, Poly2) were employed to improve predictions. This cohesive approach combined the advantages of physics-informed feature extraction (WST) and deep sequence learning (LSTM), ensuring precise and robust forecasting of battery temperature distributions.

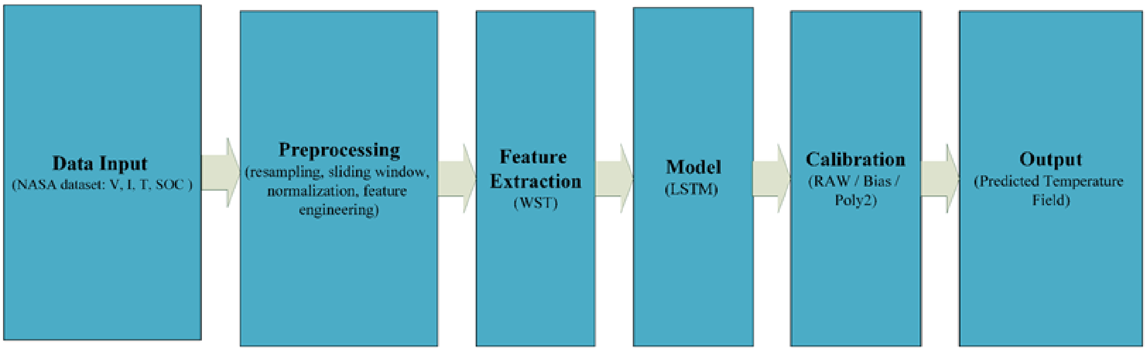

Figure 6. Architecture of the LSTM network cell.

5. Results and discussion

The efficacy of the proposed WST-LSTM model was assessed using the NASA Ames dataset and compared across several calibration procedures. Results are presented as RMSE, MAE, and R^2, accompanied by validation through scatter plots and residual histograms. Table 4 presents a comparison of the efficacy of RAW predictions, bias correction, and polynomial (Poly2) calibration.

Table 4. Summarizes the effect of calibration strategies on model performance.

Calibration Method	**RMSE (°C)**	**MAE (°C)**	**R^2**	**Notes**
RAW	1.302	1.049	0.89	Direct predictions
Bias correction	0.899	0.693	0.95	Best accuracy
Poly2	0.809	0.728	0.88	Chosen model (better stability)

Table 4 shows the effect of several calibration methods on the WST-LSTM model's predictive accuracy. The uncalibrated (RAW) projections yielded an RMSE of 1.302 °C and an R^2 of 0.89, indicating systematic bias. The application of bias correction markedly improved performance, reducing the RMSE to 0.899 °C and increasing R^2 to 0.95. Poly2 decreased the RMSE to 0.809 °C and the MAE to 0.728 °C, while preserving a R^2 of 0.88. Although its coefficient of determination was slightly lower than that of the bias-corrected model, Poly2 yielded the lowest overall error. It exhibited more stable, balanced residual distributions, as illustrated in Figures 7 and 8. Consequently, Poly2 was chosen as the definitive calibration method.

Even if the projected WST-LSTM + Poly2 setup delivered impressive results on the NASA PCoE dataset, the confirmation remained limited to a single cell chemistry and format. To thoroughly evaluate the model's resilience, additional datasets with different chemistries (e.g., LFP, NMC), cell shapes (e.g., 21700), pouch styles, and high C-rate operating conditions above 3C would be necessary. However, the feature-extraction WST was clean, and the model's stable behavior across load segments also suggested that the approach could be a viable means for battery categories, which could be further experimentally verified.

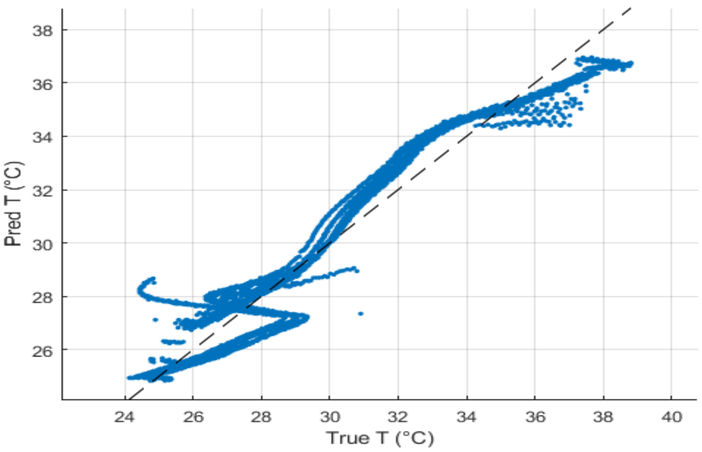

Figure 7. Scatter plot of predicted vs. actual temperatures.

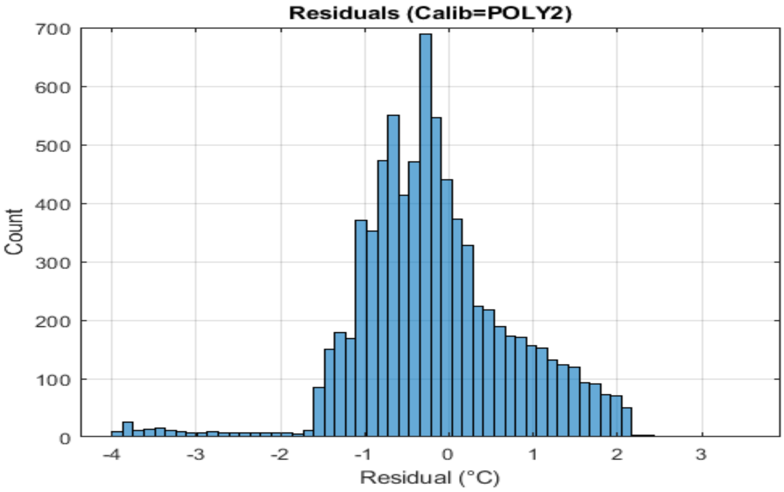

Figure 8. Residual distribution histogram.

Table 5 provides a direct comparison between the raw-signal LSTM baseline and the proposed WST-LSTM model. Incorporating WST-based representations reduced the RMSE from 1.302 °C to 0.809 °C, while the R^2 value shifted slightly from 0.89 to 0.88. These results indicated that WST preprocessing reshapes the input space into more stable, multi-scale descriptors, thereby enabling the LSTM to capture temporal patterns with reduced error. By providing a more structured representation of non-stationary signals, the WST-LSTM configuration exhibits more consistent error behavior than the unprocessed LSTM baseline.

Table 5. Comparison between baseline LSTM and proposed WST-LSTM.

Model	RMSE (°C)	MAE (°C)	R^2	Notes
LSTM (raw)	1.302	1.049	0.89	Baseline, trained on raw signals.
WST-LSTM (Poly2)	0.809	0.728	0.88	Proposed, with WST features + calibration

Figure 7 illustrates the correlation between actual temperatures (True T) and forecast temperatures (Pred T). The dashed line denotes the optimal 45° line when forecasts aligned flawlessly with the data. Most of the data points are concentrated near this line, especially within the 28–33 °C range, indicating the model's excellent precision in this range. Nonetheless, some discrepancies were evident at the extremes (below 27 °C and above 35 °C), when predictive accuracy was slightly diminished. This behavior is anticipated owing to the intrinsic non-linearities within the data.

Figure 8 illustrates the distribution of residuals derived from the battery temperature prediction model. Most residuals are clustered near zero (0 °C), indicating that most predictions were close to the actual readings. The distribution was approximately normal, with only a few outliers at ±3 °C. This affirmed the model's stability and its ability to deliver reliable forecasts in most cases.

To further interpret the role of the Wavelet Scattering Transform, an additional sensitivity inspection was performed by analyzing the relative contribution of WST paths across the zero-, first-, and second-order scattering coefficients. The analysis revealed that the first-order scattering paths, responsible for capturing fundamental and low-frequency components, carried the most significant weight in the prediction process. In contrast, second-order paths primarily contributed to high-frequency transient distortions. These observations were consistent with the WST behavior reported in prior work, where >98% of informative signal energy was concentrated in the first three scattering orders, and high-frequency invariants selectively encoded dynamic disturbances. Such structure-aligned feature concentration confirmed that WST was not functioning as a black-box enhancer but was extracting physically meaningful thermal signatures relevant to battery temperature evolution.

The RAW predictions exhibited the largest errors (RMSE = 1.302 °C, MAE = 1.049 °C, $R^2 = 0.89$), indicating substantial bias. The implementation of bias correction improved outcomes, yielding the best R^2 (0.95) and reducing errors (RMSE = 0.899 °C and MAE = 0.693 °C). Poly2 had the lowest overall errors (RMSE = 0.809 °C and MAE = 0.628 °C) and generated more stable residuals, although it had a slightly lower R^2 (0.88). This indicated that Poly2 was the most reliable choice, as it reduced errors and better managed non-linear deviations.

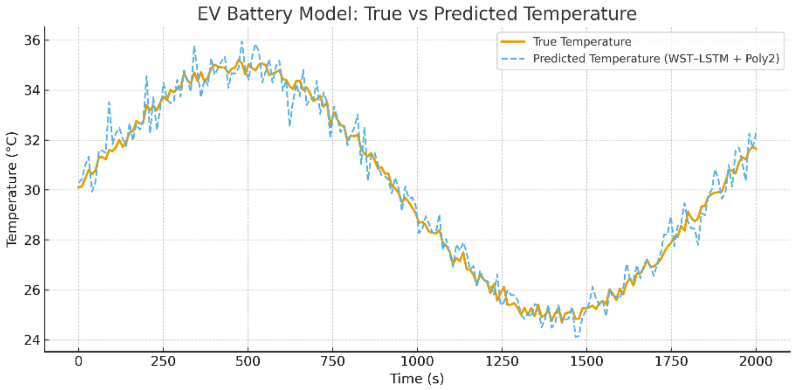

Figure 9. EV battery model: True vs predicted temperature.

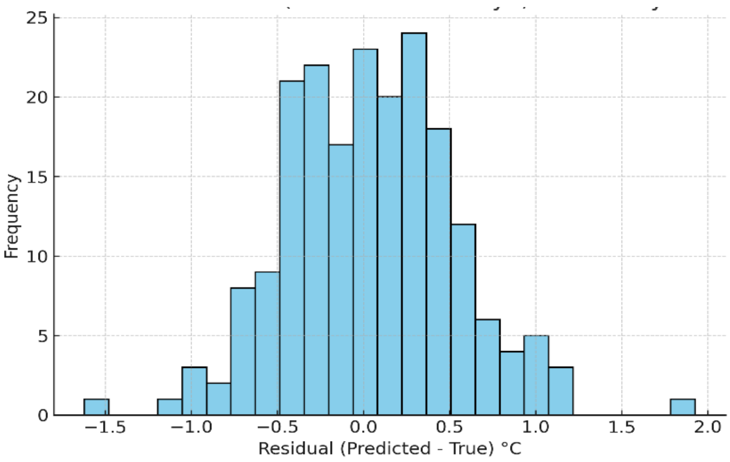

Figure 10. Residual distribution (WST-LSTM + Poly2, EV battery model).

To evaluate the generalization capability of the proposed WST-LSTM + Poly2 framework, the approach was applied to an electric vehicle battery model in MATLAB/Simulink, simulating realistic driving patterns that included variable discharge rates and regenerative braking. The model demonstrated strong predictive performance, achieving high R^2 and low RMSE and MAE, confirming its reliability under real-world EV operating conditions. Figures 9 and 10 depict the anticipated versus actual battery temperature and the distribution of residuals, respectively.

The combination of WST and LSTM showed significant efficacy beyond calibration. The WST provided translation-invariant, noise-resistant spectrum representations, whereas the LSTM captured long-term temporal dependencies. The WST-LSTM framework improved prediction accuracy and resilience compared with traditional LSTM models trained on raw signals, underscoring its significance for modeling non-stationary battery data. Significantly, these findings were corroborated across four NASA Ames benchmark cells (B0005, B0006, B0007, and B0018), thereby affirming the generalizability of the proposed methodology and its applicability across operating conditions and cell attributes.

In this study, we focused on comparing the proposed WST-LSTM + Poly2 framework with a raw-signal LSTM baseline to isolate the contribution of WST-based feature extraction. Tree-based ensemble models such as DT, ETR, LGBM, and CatBoost were not included in the experimental setup, and broader benchmarking against these architectures will be explored in future work.

The calibration analysis showed that the WST-LSTM + Poly2 configuration achieved lower overall errors and produced more stable residual distributions compared with the RAW and bias-correction baselines. When applied to the NASA dataset, Poly2 consistently reduced RMSE and MAE, demonstrating its effectiveness as a post-processing refinement method.

To further validate the model's generalization, the WST-LSTM + Poly2 framework was evaluated on a MATLAB/Simulink electric-vehicle battery model under dynamic driving conditions. The framework achieved high predictive efficiency, defined as $\eta\_pred = 100 \times R^2$, which closely reflects its performance on laboratory datasets. This consistency highlights its robustness and suitability for real-world EV battery management applications.

Our primary aim of this study was to isolate and evaluate the effect of the Wavelet Scattering Transform on the stability and precision of thermal feature extraction. Consequently, the baseline comparison centers on a raw-signal LSTM, enabling evaluation of WST's contribution without interference from architectural modifications. Although comprehensive comparisons with alternative architectures, such as CNN-LSTM, Transformer, or TCN, are beneficial, they fall outside the purview of this study. This benchmarking will be undertaken in future research to facilitate a comprehensive architectural assessment once multi-architecture training and tuning can be executed under uniform experimental settings.

It is important to note that we did not perform strict leave-one-cell-out (LOCO) validation. While the current group-aware split prevents cycle-level leakage, complete LOCO testing (e.g., training on B0005 and B0018 and evaluating on unseen cells such as B0006 or B0007) requires harmonized multi-cell datasets with consistent operating profiles. This limitation has been acknowledged and will be addressed in future work.

Moreover, we focused on isolating and assessing the impact of the WST on the stability and accuracy of thermal feature extraction. As a result, the baseline comparison focuses primarily on a raw-signal LSTM, enabling evaluation of WST's contribution without the effects of architectural changes. While thorough comparisons across topologies such as CNN-LSTM, Transformer, and Temporal Convolutional Network (TCN) would be advantageous, they are beyond the scope of this study. Such benchmarking will be conducted in subsequent work to enable a comprehensive architectural review, enabling multi-architecture training and tuning to be carried out under the same experimental conditions.

Moreover, in future work, we will investigate resilient explainability techniques to provide coherent and interpretable insights into model predictions. Expanding the proposed methodology to include supplementary battery data (e.g., discharge rates, aging effects) and operational scenarios may facilitate broader applicability in BMS. Specifically, leveraging the framework for electric vehicle platforms will be crucial to advancing next-generation energy storage systems and ensuring greater safety and performance in practical applications.

6. Conclusions

This study is confined to single-point temperature forecasting and does not simulate geographic temperature distributions. Expanding the framework to encompass multi-point or field-level estimation is a prospective avenue for further exploration. We introduced an innovative hybrid framework that combines the WST with LSTM networks and a Polynomial (Poly2) calibration method to tackle the issue of LIB temperature prediction. The methodology leverages the strengths of each component: WST extracts translation-invariant, noise-resistant spectral features from raw signals; LSTM captures long-term temporal dependencies in charge-discharge cycles; and Poly2 calibration reduces residual errors and rectifies nonlinear deviations. Collectively, these elements constitute a holistic strategy that improves predictive precision and stability.

The proposed WST-LSTM + Poly2 framework was designed to capture better sequential dependencies and spectral variations inherent in battery thermal behavior. While tree-based ensemble models are widely used and offer computational efficiency and interpretability, they were not included in the comparative evaluation in this study. Our focus of this work is on demonstrating the contribution of WST-based feature extraction relative to a raw-signal LSTM baseline. In future work, we will explore broader benchmarking against architectures such as LightGBM, TCN, and Transformer.

Validation was conducted using several NASA Ames cells (B0005, B0006, B0007, and B0018) and an electric vehicle battery model in MATLAB/Simulink, confirming that the proposed approach generalizes effectively beyond the training data. This provides compelling evidence that the framework is precise and practically feasible for real-world applications.

In conclusion, the WST-LSTM + Poly2 framework offers a dependable approach for enhanced thermal safety evaluation and (BMS) applications. Its capacity to provide accurate, consistent, and generalizable forecasts positions it as a strong candidate for integration into electric vehicles and advanced energy storage systems, thereby enhancing the safety, reliability, and longevity of lithium-ion batteries.

This work is limited to single-point temperature prediction and does not attempt to reconstruct spatial temperature fields. Extending the proposed framework to multi-sensor or field-level thermal estimation is left for future research.

In future work, we will extend the proposed framework to additional battery chemistries, cell formats, and high-C-rate operating conditions to rigorously evaluate its generalization capability. We will incorporate strict leave-one-cell-out validation to assess cell-to-cell robustness.

Use of AI tools declaration

The authors declare they have not used Artificial Intelligence (AI) tools in the creation of this article.

Conflict of interest

There are no conflicts of interest with any party.

Author contributions

Conceptualization, Mohamed M. A. Hassan; Methodology, Hatem Kayed, and Bassam Adel; Data curation, Hatem Kayed, and Bassam Adel; Writing—original draft preparation, Mohamed M. A. Hassan; Writing—review and editing, all authors. All authors have read and agreed to the published version of the manuscript.

References

1. Han J, Wang F (2023) Design and testing of a small orchard tractor driven by a power battery. *Eng Agríc* 43: e20220195. https://doi.org/10.1590/1809-4430-eng.agric.v43n2e20220195/2023
2. Huang Y, Li J (2022) Key challenges for grid-scale lithium-ion battery energy storage. *Adv Energy Mater* 12: 2202197. https://doi.org/10.1002/aenm.202202197
3. Yang S, Ling C, Fan Y, et al. (2019) A review of lithium-ion battery thermal management system strategies and the evaluation criteria. *Int J Electrochem Sci* 14: 6077–6107. https://doi.org/10.20964/2019.07.06
4. Feng X, Zheng S, Ren D, et al. (2019) Investigating the thermal runaway mechanisms of lithium-ion batteries based on thermal analysis database. *Appl Energy* 246: 53–64. https://doi.org/10.1016/j.apenergy.2019.04.009

5. Gharebaghi M, Rezaei O, Li C, et al. (2024) A survey on using second-life batteries in stationary energy storage applications. *Energies* 18: 42. https://doi.org/10.3390/en18010042
6. Zeng Y, Chalise D, Lubner SD, et al. (2021) A review of thermal physics and management inside lithium-ion batteries for high energy density and fast charging. *Energy Storage Mater* 41: 264–288. https://doi.org/10.1016/j.ensm.2021.06.008
7. Smith K, Wang CY (2006) Power and thermal characterization of a lithium-ion battery pack for hybrid-electric vehicles. *J Power Sources* 160: 662–673. https://doi.org/10.1016/j.jpowsour.2006.01.038
8. Wang Q, Ping P, Zhao X, et al. (2012) Thermal runaway caused fire and explosion of lithium-ion battery. *J Power Sources* 208: 210–224. https://doi.org/10.1016/j.jpowsour.2012.02.038
9. Feng X, Ouyang M, Liu X, et al. (2018) Thermal runaway mechanism of lithium-ion battery for electric vehicles: A review. *Energy Storage Mater* 10: 246–267. https://doi.org/10.1016/j.ensm.2017.05.013
10. Tran MK, Mevawalla A, Aziz A, et al. (2022) A review of lithium-ion battery thermal runaway modeling and diagnosis approaches. *Processes* 10: 1192. https://doi.org/10.3390/pr10061192
11. Pal S, Kashyap P, Panda B, et al. (2025) A comprehensive review of thermal runaway for batteries: Experimental, modelling, challenges and proposed framework. *Int J Green Energy*, 1–24. https://doi.org/10.1080/15435075.2025.2462606
12. Chalise D, Lu W, Srinivasan V, et al. (2020) Heat of mixing during fast charge/discharge of a Li-ion cell: A study on NMC523 cathode. *J Electrochem Soc* 167: 090560. https://doi.org/10.1149/1945-7111/abaf71
13. Goodenough JB, Park KS (2013) The Li-ion rechargeable battery: A perspective. *J Am Chem Soc* 135: 1167–1176. https://doi.org/10.1021/ja3091438
14. Bandhauer TM, Garimella S, Fuller TF (2011) A critical review of thermal issues in lithium-ion batteries. *J Electrochem Soc* 158: R1. https://doi.org/10.1149/1.3515880
15. Spotnitz R (2003) Simulation of capacity fade in lithium-ion batteries. *J Power Sources* 113: 72–80. https://doi.org/10.1016/S0378-7753(02)00490-1
16. Pesaran AA (2002) Battery thermal models for hybrid vehicle simulations. *J Power Sources* 110: 377–382. https://doi.org/10.1016/S0378-7753(02)00200-8
17. Sheikh SS, Anjum M, Khan MA, et al. (2020) A battery health monitoring method using machine learning: A data-driven approach. *Energies* 13: 3658. https://doi.org/10.3390/en13143658
18. Balouji E, Salor O (2017) Classification of power quality events using deep learning on event images. *2017 3rd International Conference on Pattern Recognition and Image Analysis (IPRIA)*, Shahrekord, Iran, 216–221. https://doi.org/10.1109/PRIA.2017.7983049
19. Graves A, Mohamed AR, Hinton G (2013) Speech recognition with deep recurrent neural networks. *2013 IEEE International Conference on Acoustics, Speech, and Signal Processing (ICASSP)*, Vancouver, BC, Canada, 6645–6649. https://doi.org/10.1109/ICASSP.2013.6638947
20. Xu K, Zhuang J, Meng X, et al. (2023) Temperature-field prediction for lithium-ion batteries using improved local tangent space alignment. *Int J Heat Mass Transfer* 209: 124126. https://doi.org/10.1016/j.ijheatmasstransfer.2023.124126
21. Mallat S (2012) Group invariant scattering. *Commun Pure Appl Math* 65: 1331–1398. https://doi.org/10.1002/cpa.21413

22. Ramamoorthy ML, Selvaperumal S, Nagarajan R (2025) An adaptive battery health monitoring framework using wavelet scattering and spiking graph transformers optimized by arctic wolf algorithm. *Iran J Sci Technol, Trans Electr Eng*, 1–27. https://doi.org/10.1007/s40998-025-00885-4
23. NASA (2012) Prognostics Center of Excellence (PCoE) Data Set Repository. Available from: https://www.nasa.gov/intelligent-systems-division/discovery-and-systems-health/pcoe/pcoe-data-set-repository/.
24. Liu N, Zhang F, Chang L, et al. (2024) Scattering-based hybrid network for facial attribute classification. *Front Comput Sci* 18: 183313. https://doi.org/10.1007/s11704-023-2570-6
25. Wang Y, Guo P, Ma N, et al. (2022) Robust wavelet transform neural-network-based short-term load forecasting for power distribution networks. *Sustainability* 15: 296. https://doi.org/10.3390/su15010296
26. Khumprom P, Yodo N (2019) A data-driven predictive prognostic model for lithium-ion batteries based on a deep learning algorithm. *Energies* 12: 660. https://doi.org/10.3390/en12040660
27. He T, Gong Z (2024) State of health estimation for lithium-ion batteries using a hybrid neural network model with multi-scale convolutional attention mechanism. *J Power Sources* 609: 234680. https://doi.org/10.1016/j.jpowsour.2024.234680
28. Mansour NM, Awaad IA, Abdelsalam AA (2024) Performance analysis of wavelet scattering transform-based feature matrix for power system disturbances classification. *Int J Electr Comput Eng* 14: 6094–6110. https://doi.org/10.11591/ijece.v14i6.pp6094-6110
29. Mansour NM, Abdelsalam AA, Awaad IA, et al. (2025) A novel long short-term memory-based approach for microgrid fault detection and classification using the wavelet scattering transform. *IEEE Access* 13 : 120905–120916. https://doi.org/10.1109/ACCESS.2025.3584355
30. Wang B, Chen Z, Zhang P, et al. (2025) The lithium-ion battery temperature field prediction model based on CNN-Bi-LSTM-AM. *Sustainability* 17: 2125. https://doi.org/10.3390/su17052125
31. Xu K, Zhuang J, Meng X, et al. (2023) Temperature-field prediction for lithium-ion batteries using improved local tangent space alignment. *Int J Heat Mass Transfer* 209: 124126. https://doi.org/10.1016/j.ijheatmasstransfer.2023.124126
32. Zhou X, Guo W, Shi X, et al. (2024) Machine learning assisted multi-objective design optimization for battery thermal management system. *Appl Therm Eng* 253: 123826. https://doi.org/10.1016/j.applthermaleng.2024.123826
33. Sherkatghanad Z, Ghazanfari A, Makarenkov V, et al. (2024) A self-attention-based CNN-Bi-LSTM model for accurate state-of-charge estimation of lithium-ion batteries. *J Energy Storage* 88: 111524. https://doi.org/10.1016/j.est.2024.111524
34. Bruna J, Mallat S (2013) Invariant scattering convolution networks. *IEEE Trans Pattern Anal Mach Intell* 35: 1872–1886. https://doi.org/10.1109/TPAMI.2012.230
35. Andén J, Mallat S (2011) Multiscale scattering for audio classification. *Proc 12th Int Soc Music Information Retrieval Conf (ISMIR)*, 657–662. https://doi.org/10.5281/zenodo.1415750
36. Bruna J, Mallat S (2013) Invariant scattering convolution networks. *IEEE Trans Pattern Anal Mach Intell* 35: 1872–1886. https://doi.org/10.1109/TPAMI.2012.230
37. Andén J, Mallat S (2014) Deep Scattering Spectrum. *IEEE Trans Signal Process* 62: 4114–4128. https://doi.org/10.1109/TSP.2014.2326991

38. Bruna J, Mallat S (2011) Classification with scattering operators. *CVPR 2011*, 1561–1566. https://doi.org/10.1109/CVPR.2011.5995635
39. Zarka J, Thiry L, Angles T, et al. (2019) Deep network classification by scattering and homotopy dictionary learning. *arXiv*. https://doi.org/10.48550/arXiv.1910.03561
40. AlBader M, Toliyat HA (2020) Wavelet scattering transform based induction motor current signature analysis. *2020 International Conference on Electrical Machines (ICEM)*, 1452–1457. https://doi.org/10.1109/ICEM49940.2020.9270810
41. Al-Itbi AS, Alwahhab ABA, Sahan AM (2022) X-Ray Covid-19 detection based on scatter wavelet transform and dense deep neural network. *Comput Syst Sci Eng* 41: 3. https://doi.org/10.32604/csse.2022.021980
42. Susu AA, Agboola HA, Solebo C, et al. (2020) Wavelet time scattering based classification of interictal and preictal EEG signals. *J Brain Res* 3: 115. https://doi.org/10.37421/2684-4583.2020.3.115
43. Liu F, Xia S, Wei S, et al. (2022) Wearable electrocardiogram quality assessment using wavelet scattering and LSTM. *Front Physiol* 13: 905447. https://doi.org/10.3389/fphys.2022.905447
44. Agboola HA, Zaccheus JE (2023) Wavelet image scattering-based glaucoma detection. *BMC Biomed Eng* 5: 1. https://doi.org/10.1186/s42490-023-00067-5
45. Hirn M, Mallat S, Poilvert N (2017) Wavelet scattering regression of quantum chemical energies. *Multiscale Model Simul* 15: 2. https://doi.org/10.1137/16M1075454
46. Rohan A (2022) Deep scattering spectrum germaneness for fault detection and diagnosis for component-level Prognostics and Health Management (PHM). *Sensors* 22: 9064. https://doi.org/10.3390/s22239064
47. Lai WH, Tsai ST, Cheng DL, et al. (2021) Application of wavelet scattering and machine learning on structural health diagnosis for quadcopter. *Appl Sci* 11: 10297. https://doi.org/10.3390/app112110297
48. de Aguiar EL, Lazzaretti AE, Mulinari BM, et al. (2021) Scattering transform for classification in non-intrusive load monitoring. *Energies* 14: 6796. https://doi.org/10.3390/en14206796
49. Bourgana T, Brijder R, Ooijevaar T, et al. (2021) Wavelet scattering network based bearing fault detection. *Proceedings of the European Conference of the PHM Society* 6: 8. https://doi.org/10.36001/phme.2021.v6i1.2875
50. The MathWorks Inc (2022) MATLAB version: 9.13.0 (R2022b), Natick, Massachusetts. Available from: https://www.mathworks.com.
51. Hochreiter S, Schmidhuber J (1997) Long Short-Term Memory. *Neural Comput* 9: 1735–1780. https://doi.org/10.1162/neco.1997.9.8.1735
52. Abdelsalam AA, Hassanin AM, Hasanien HM (2021) Categorisation of power quality problems using long short-term memory networks. *IET Gener Transm Distrib* 15: 1626–1639. https://doi.org/10.1049/gtd2.12122
53. Liu Y, Wang Y, Yang X, et al. (2017) Short-term travel time prediction by deep learning: A comparison of different LSTM-DNN models. *2017 IEEE 20th International Conference on Intelligent Transportation Systems* (ITSC). https://doi.org/10.1109/ITSC.2017.8317886
54. Balouji E, Salor O (2017) Classification of power quality events using deep learning on event images. *2017 3rd International Conference on Pattern Recognition and Image Analysis (IPRIA)*. https://doi.org/10.1109/PRIA.2017.7983049

55. Zhang L, Zhu X, Zhao S, et al. (2017) A novel virtual network fault diagnosis method based on long short-term memory neural networks. *2017 IEEE 86th Vehicular Technology Conference (VTC-Fall)*. https://doi.org/10.1109/VTCFall.2017.8288236
56. Chauhan S, Vig L (2015) Anomaly detection in ECG time signals via deep long short-term memory networks. *2015 IEEE International Conference on Data Science and Advanced Analytics (DSAA)*. https://doi.org/10.1109/DSAA.2015.7344872

AIMS Press